AGU PUBLICATIONS

JGR

Journal of Geophysical Research: Oceans

RESEARCH ARTICLE

10.1002/2014JC010030

Special Section:
Early scientific results from the salinity measuring satellites Aquarius/SAC-D and SMOS

# Coherent evidence from Aquarius and Argo for the existence of a shallow low-salinity convergence zone beneath the Pacific ITCZ

**Lisan Yu**[1]

[1]Department of Physical Oceanography, Woods Hole Oceanographic Institution, Woods Hole, Massachusetts, USA

**Abstract** Aquarius observations feature a prominent zonal sea-surface salinity (SSS) front that extends across the tropical Pacific between 2–10°N. By linking to Argo subsurface salinity observations and satellite-derived surface forcing datasets, the study discovered that the SSS front is not a stand-alone feature; it is in fact the surface manifestation of a low-salinity convergence zone (LSCZ) located within 100 m of the upper ocean. The near-surface salinity budget analysis suggested that, although the LSCZ is sourced from the rainfall in the Inter-tropical convergence zone (ITCZ), its generation and maintenance are governed by the wind-driven Ekman dynamics, not the surface evaporation-minus-precipitation flux. Three distinct features highlight the relationship between the oceanic LSCZ and the atmospheric ITCZ. First, the seasonal movement of the LSCZ is characterized by a monotonic northward displacement starting from the near-equatorial latitudes in boreal spring, unlike the ITCZ that is known for its seasonal north-south displacement. Second, the lowest SSS waters in the LSCZ are locked to the northern edge of the Ekman salt convergence throughout the year, but have no fixed relationship with the ITCZ rain band. Collocation between the LSCZ and ITCZ occurs only during August-October, the time that the ITCZ rain band coincides with the Ekman convergence zone. Lastly, the SSS front couples with the Ekman convergence zone but not the ITCZ. The evidence reinforces the findings of the study that the Ekman processes are the leading mechanism of the oceanic LSCZ and the SSS front is the surface manifestation of the LSCZ.

**Key Points:**
- Aquarius observations showed a prominent zonal SSS front under the Pacific ITCZ.
- Argo showed that the SSS front manifested a low-salinity convergence zone (LSCZ).
- The LSCZ was governed by the wind-driven Ekman processes, not the ITCZ rain.

**Correspondence to:**
L. Yu,
lyu@whoi.edu

**Citation:**
Yu, L. (2014), Coherent evidence from Aquarius and Argo for the existence of a shallow low-salinity convergence zone beneath the Pacific ITCZ, *J. Geophys. Res. Oceans*, *119*, 7625–7644, doi:10.1002/2014JC010030.

Received 7 APR 2014
Accepted 8 OCT 2014
Accepted article online 10 OCT 2014
Published online 18 NOV 2014

## 1. Introduction

The Aquarius/SAC-D mission launched in June 2011 has revolutionized our ability to observe the global sea surface salinity (SSS) on a routine and timely basis. At present, the Aquarius measurements provide complete global coverage every 7 days with a footprint resolution between 90 and 150 km across a ~390 km-wide swath [*Lagerloef et al*., 2008]. The Aquarius mission together with the European Soil Moisture/Ocean Salinity (SMOS) mission that was launched in November 2009 [*Font et al*., 2010; *Reul et al*., 2014a, 2014b] offers an unprecedented opportunity for studying SSS variability on many spatial and temporal scales, from the basinwide salinity maxima and minima centers [*Qu et al*., 2011; *Alory et al*., 2012], through the tropical instability waves [*Lee et al*., 2012] and the Madden-Julian Oscillations [*Grunseich et al*., 2013], and down to the surface freshwater plumes generated by the tropical cyclone [*Grodsky et al*., 2012] or excessive river runoff [*Gierach et al*., 2013]. The phenomena in most of these studies are examined using the mean and anomalous SSS fields, as the topical SSS features are distinctive and readily recognizable. However, for studies that focus on the distribution of water masses and their properties around the global oceans, the SSS gradient field would be a more desirable variable to start with. The narrow zones of enhanced horizontal gradients, often referred to as fronts, are the characteristic manifestation of the convergence zones of two water masses with different salinities. The disposition of the SSS fronts and the contrasts across the fronts bear important information for unraveling the near-surface processes contributing to the generation, circulation, and distribution of surface water masses [*Emery*, 2003].

Surface water masses and types are generally formed by direct interaction and exchange between the ocean and the atmosphere and between the open-ocean and coastal waters. Satellite observations have revealed the existence of SSS fronts in both the extratropical (poleward of 25° north and south) and the tropical oceans. *Reul et al*. [2014a] described the prominent SSS front in the vicinity of the Gulf Stream, showing that the collision between the cold, fresh slope and shelf waters and the warm, saline central waters leads to sharp SSS gradients meandering along the path of the warm currents. Strong SSS gradients

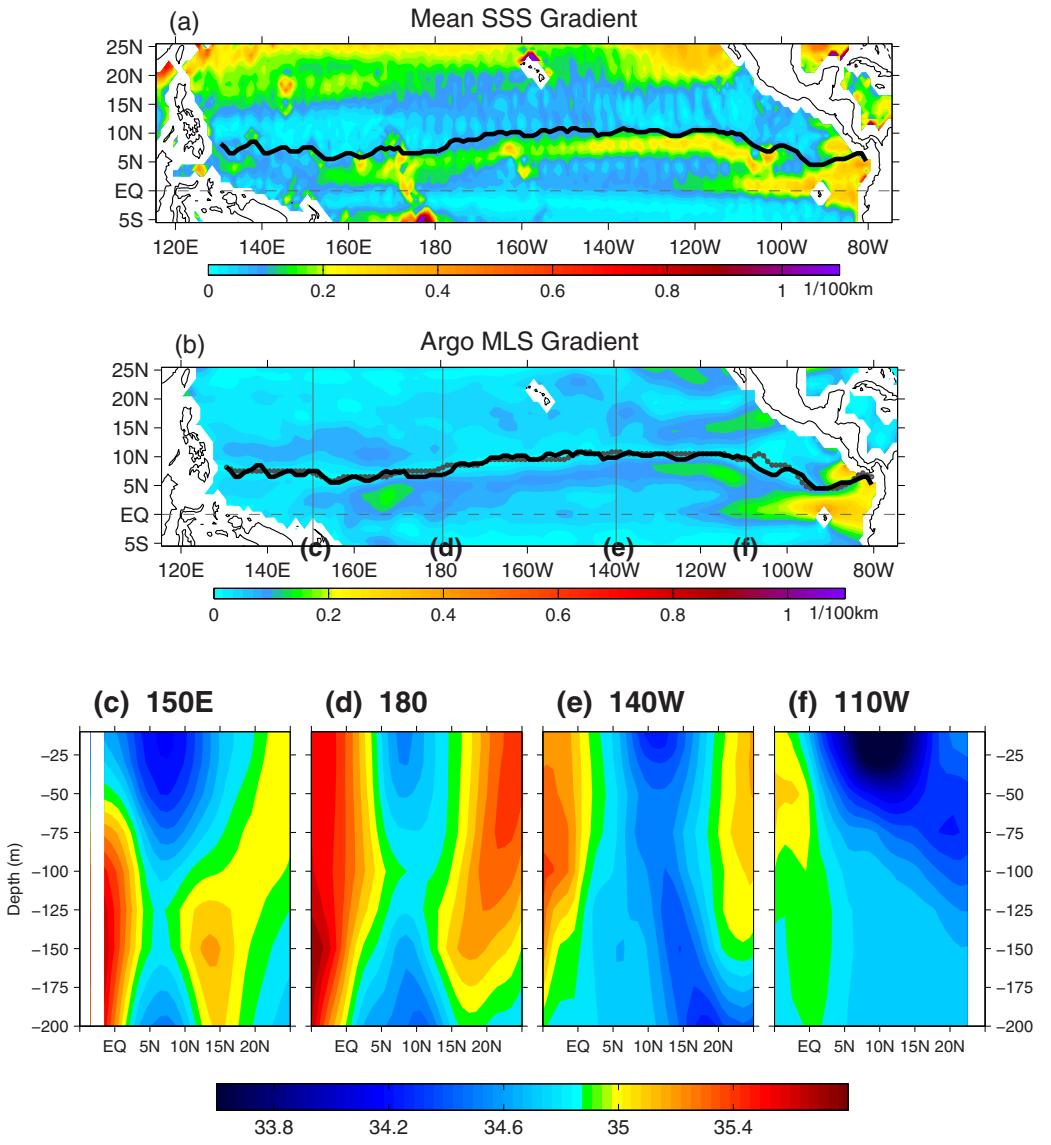


**Figure 1.** Magnitude of the surface salinity gradients constructed from (a) Aquarius SSS observations and (b) Argo MLS. The location of Aquarius Smin (black line) is superimposed in both (a) and (b), while the location of the Argo MLS minima (thick gray) is superimposed in (b). The letters c, d, e and f on the *x* axis in (b) and the associated meridians marked by gray lines denote the locations of the salinity vertical section of the upper 200m along (c) 150°E, (d) 180, (e) 140°W, and (f) 110°W. All fields were based on the Aquarius 2 year observing period from September 2011 to August 2013.

are also featured in regions that are adjacent to continental freshwater discharges, such as the Amazon/Orinoco discharge plumes in the western tropical Atlantic [e.g., *Salisbury et al.*, 2011] and the Ganges-Brahmaputra river discharges in the Bay of Bengal [*Papa et al.*, 2010]. By comparison, the tropical SSS fronts are more zonally oriented, with the longest and most prominent one extending across the tropical Pacific at a few degrees north of the equator (Figure 1a). The fronts in the other tropical basins are comparably shorter, with a spatial extent typically about 30–40° in longitude (not shown). All the tropical SSS fronts have one feature in common, that is, they are located in close proximity to the rain belt of the Intertropical Convergence Zone (ITCZ). Given that a SSS front represents a boundary that separates the surface water masses of different salinities, it is intuitively plausible that the formation mechanism of the SSS front beneath the ITCZ resides in the interaction between the fresh rainfall water and the saline ocean surface water.

Ocean salinity is regarded as an important source of observations for the global water cycle. The close connection between the salinity and the evaporation-minus-precipitation (hereafter E-P) flux at several spatial

and temporal scales illuminates the possibility of using the ocean as a rain gauge [*Elliott*, 1974] to monitor the change of the ocean water cycle [*Font et al*., 2010; *Lagerloef et al*., 2010; *Durack and Wijffels*, 2010; *Yu*, 2010; *Terray et al*., 2012; *Vinogradova and Ponte*, 2013; *Reul et al*., 2014b]. Evaporation and precipitation over the oceans are key components of the global water cycle. However, unlike salinity that is observed both directly from in situ and remotely from satellites, evaporation and precipitation are parameterized or derived from relevant geophysical variables that can be observed. Presently, the estimates of their mean distribution and variations contain large biases [*Adler et al*., 2003; *Yu and Weller*, 2007]. The pressing need to improve the quantification and characterization of the change of the global water cycle in response to the changing climate has been a main incentive in advancing the use of the ocean as a rain gauge. Despite the efforts, extracting the freshwater information directly from salinity measurements [*Elliott*, 1974; *Short et al*., 1997; and *Wijesekera et al*., 1999] is challenged by the fact that the relationship between SSS and E-P is not linear. Oceanic processes, including advection, entrainment, and mixing, are a major contributor to SSS variability on a wide range of temporal scales [*Delcroix and Henin*, 1991; *Delcroix et al*., 1996; *Johnson et al*., 2002; *Reverdin et al*., 2007; *Foltz and McPhaden*, 2008; *Yu*, 2011] Additionally, unlike the surface heat flux that serves as both forcing and damping mechanisms for sea surface temperature (SST), the E-P flux forces the SSS anomalies but does not damp them. The SSS anomalies tend to be more persistent than the SST anomalies and are more strongly modified by oceanic advection and mixing.

Quantifying the contributions of the surface E-P flux and oceanic processes to near-surface salinity variability has been conducted from both observational [e.g., *Delcroix and Henin*, 1991; *Johnson et al*., 2002; *Reverdin et al*., 2007; *Foltz and McPhaden*, 2008] and modeling [e.g., *Mignot and Frankignoul*, 2003] perspectives. To gain a clear depiction of the influence regime of all the contributing terms, *Yu* [2011] computed the covariance between each of the forcing processes (e.g., E-P, ocean advection by the wind-driven Ekman currents, the geostrophic currents, the vertical entrainment, and mixing) and SSS seasonal variability and assembled a global forcing regime map based on the largest magnitude of the convariance. The forcing regime map thus obtained shows an intriguing yet compelling pattern [*Yu*, 2011, Figure 9]. The E-P flux reigns only in the areas associated with the ITCZ and SPCZ rain bands, while the wind-driven Ekman salt transport has a more broad dominance, covering large areas of the tropical and subtropical regions. In light of the omnipresence of ocean advection in near-surface salinity variability that is found in many studies [e.g., *Delcroix and Henin*, 1991; *Johnson et al*., 2002; *Reverdin et al*., 2007; *Foltz and McPhaden*, 2008; *Ren and Riser*, 2009; *Bingham et al*., 2010], the regime map obtained by *Yu* [2011] is not a surprise, but a coherent manifestation of the complex interaction of the fresh rainfall water with the saline surface water and the surface currents.

The rain that falls on the ocean surface does not stay locally. The fresh water is a mass flux, which adds to the mass of the water column and causes a pressure perturbation [*Lorbacher et al*., 2012] and fast oceanic responses in terms of gravity waves and barotropic Rossby waves. The theoretical model experiments conducted by *Huang and Jin* [2002] showed that the effect of the barotropic Rossby waves excited by the rain-induced pressure perturbation can be perceived over the global basin in a matter of days. Meanwhile, the zero-salt water left behind would mix with the ambient salty water, affecting the near-surface salinity and leading to the formation of salinity phenomena that are unique to the ocean surface layer. Some of the known salinity phenomena in the tropical ocean include the salinity-stratified barrier layer [*Lukas and Lindstrom*, 1991], the "fresh equatorial jets" near the dateline in the western Pacific [*Roemmich et al*., 1994], the salinity signature of the tropical instability waves [*Lee et al*., 2012], and the fresh pools in the western and eastern Pacific [*Hénin et al*., 1998; *Alory et al*., 2012; *Maes and O'Kane*, 2014]. The low-salinity surface waters also lead to marked SSS fronts in the vicinity of the tropical rain bands. However, few studies to date have examined how these tropical SSS fronts are generated, what are the subsurface structure associated with the fronts, and what is the relation of the fronts to the near-surface ocean circulation. These issues are important. The tropical rain region receives more than 450 cm of precipitation on the annual mean basis [*Adler et al*., 2003; *Joyce et al*., 2004], the venue that this large body of the freshwater interacts with and circulates along with the ocean near-surface currents is yet to be fully understood. In this regard, the SSS fronts in the vicinity of the ITCZ hold promise of shedding important new light on the near-surface ocean processes involved in distributing the surface freshwater input on the timescales that can be resolved by the present capability of satellite observations.

The present study aims to identify and understand the mechanisms that govern the seasonal dynamics of the SSS front in the Pacific. The study is organized as follows. Section 2 describes the method and data sets

in use. Section 3 presents the analysis of the subsurface structure and seasonal characteristics of the SSS front. Section 4 discusses the processes that generate, maintain, and regulate the SSS front. The summary and conclusion are given in section 5.

## 2. Data

The analysis in this study was based on the seasonal cycles constructed from the two-year Aquarius observing period from September 2011 to August 2013. In addition to satellite SSS observations, the Argo subsurface observations and satellite-derived surface forcing products were also used to aid in the analysis. The list of data sets and description of their use in the analysis are provided below.

1. Aquarius SSS: the data set was taken from the Aquarius/SAC-D Level-2 Combined Active-Passive (CAP) version 2.0 product [*Yueh and Chaubell*, 2012]. The CAP algorithm simultaneously retrieves salinity, wind speed, and wind direction by minimizing the sum of squared differences between the geophysical transfer function and observations. The SSS front revealed by the Aquarius observations provided the motivation of the study.
2. Argo subsurface salinity and temperature fields: the 1° gridded monthly fields were processed by the Argo group at the Japan Agency for Marine-Earth Science and Technology (JAMSTEC) using a two-dimensional optimal interpolation on pressure surface [*Hosoda et al*., 2008]. The subsurface fields are available at 25 pressure levels, from 2000 to 10 dbar below the surface. The Argo observations were the key data sets in understanding the subsurface salinity structure associated with the SSS front. They were also used to derive the mixed-layer depth ($h$) for the salinity budget analysis. The mixed-layer depth was determined from a density criterion, i.e., $h$ is determined as the depth at which density is 0.125 kg $m^{-3}$ higher than the surface density [*de Boyer Montégut et al*., 2004].
3. Precipitation ($P$): the data set was the 0.25° gridded multisatellite precipitation analysis 3B43 product (version 7), which was obtained from merging the Tropical Rainfall Measuring Mission (TRMM) with precipitation estimates of other satellites [*Hoffman et al*., 2007]. The data set was used to map the relationship between the ITCZ rainfall and low-salinity surface waters and to establish the E-P flux for the salinity budget analysis.
4. Evaporation ($E$): the evaporation data set was taken from Version 3 products of the Objectively Analyzed air-sea Fluxes (OAFlux) project [*Yu and Weller*, 2007; *Yu et al*., 2008]. The data set was used together with the TRMM precipitation to form the E-P flux for the salinity budget analysis.
5. Wind stress ($\tau$): the wind stress data set was taken from the OAFlux satellite-based, 0.25° gridded, daily global vector wind analysis developed from a multisensor synthesis [*Yu and Jin*, 2012, 2014]. The product is currently available from July 1987 to December 2013. The wind stress data were needed to compute the Ekman currents.
6. Mean dynamic topography: the time-averaged global mean sea surface height for the period 1992–2002 was developed from a joint analysis of drifter, satellite altimeter, wind, and the GRACE Gravity Model-01 data by *Niiler et al*., [2003] and *Maximenko et al*., [2009]. The data set was used to compute the mean geostrophic currents.
7. Sea surface height ($\eta$): altimeter measurements of sea surface height from AVISO (http://www.aviso.oceanobs.com/es/data/index.htm) with respect to the mean of 1992–2002 were a base data set for computing the geostrophic current anomalies.

## 3. Surface and Subsurface Structures of the SSS Front

### 3.1. Relationship Between the SSS Minima and the SSS Front

The Aquarius SSS gradient field featured a prominent SSS front in the tropical Pacific Ocean that extended across the basin at latitudes between 2 and 10°N (Figure 1a). The front was located near the equator west of 160°E, and shifted progressively northward across the central Pacific, reaching the northernmost position at about 10°N near 120°W. Further eastward, the front veered southward and merged with an equatorial SSS front that stretched from the coast of South America westward to about 120°W. Meanwhile, some

short-scale localized SSS fronts were present, the most noted of which was the one centered around 7–8°N near the coast of Central America with a westward extension of about 15°.

The SSS front was intrinsically linked to the low-salinity surface waters in the region. When superimposing the location of the SSS minima onto the SSS gradient field (Figure 1b), the freshest surface water was found to reside at the northern edge of the SSS front. The connection suggested that the front was likely a boundary between the freshest surface waters and the waters that were less fresh. In light of the close proximity of the ITCZ influence, the source of the surface waters of the lowest salinity should come from the ITCZ rains.

### 3.2. Subsurface Structure of the SSS Front: Existence of a Shallow Low-Salinity Convergence Zone

From the conventional point of view, a SSS front represents a zone that converges water masses with different salinities. Such convergence would push low-salinity surface waters into the subsurface and result in a freshening of the upper ocean layer. To detect low-salinity signals in the near-surface layer under the Aquarius SSS front, the salinity fields derived from the Argo observations were examined. One major difference between the Argo surface salinity observations [*Riser et al*., 2008] and the Aquarius SSS observations is the measurement depth, as the former is commonly measured at a depth of 1 m or more (most frequently 4–5 m) below the sea surface and the latter is the skin salinity taken within the microwave penetration depth of ~1cm [*Lagerloef et al*., 2008; *Yu*, 2010]. Before proceeding to the Argo subsurface salinity structures, the consistency between Argo and Aquarius salinity measurements in characterizing the basin-scale surface frontal structure was evaluated. The Argo mixed-layer salinity (MLS) was used to represent the near-surface salinity. The MLS gradient was constructed (Figure 1b), onto which the locations of the Argo MLS minima and the Aquarius *Smin* were superimposed. The weak Argo MLS gradients were noticed, likely due to the coarse resolution of the Argo measurements—as the floats were distributed roughly every 3° [*Riser et al*., 2008]. Without the Aquarius SSS front as a reference, the front under the ITCZ could hardly be appreciated when using Argo. Despite being weak, the Argo MLS front showed a similar spatial extent and similar northeastward shift of the front location. The complete alignment between the location of the Argo MLS minima and that of the Aquarius SSS minima provided addition evidence in showing that Argo and Aquarius observations were consistent in capturing the mean features in the near-surface salinity field although the salinity signals from Argo were relatively weaker.

Four meridional sections, 150°E, 180, 140°W, and 110°W, were chosen to examine the subsurface salinity structure from the near-surface down to the depth of 200 meters (Figures 1c–1f). These four sections had a latitudinal extent from 5°S to 25°N and were used to represent the salinity subsurface structure in the western, central, and eastern portions of the tropical Pacific, respectively. The single feature that was most conspicuous in all four sections was the shallow cell of low-salinity waters in the upper 100 m. The core of the cell, i.e., the freshest waters, shifted progressively northward when extending across the basin. It was located near 6°N along 150°E, around 8°N along the dateline, and around 10°N along 140°W. When moving farther east into the eastern fresh water pool, the core veered southward to about 8°N at 110°W.

The intensity and width of the shallow, low-salinity cells varied across the basin. The cell at the dateline was weakest and narrowest. To the east of the dateline, the cells became fresher, wider, and shallower toward the east. The low-salinity cell was most intense along 110°W, the region known as the eastern Pacific fresh pool. To the west of the dateline where the western Pacific fresh pool locates, the cell became fresher, wider, and deeper. The zonal variations of the cells indicated that the enhanced freshening in the fresh pools on the two side of the basin broadened the surface salinity fronts there but may not necessarily lead to an enhanced intensity.

Despite the variations in strength, the shallow, low-salinity cell existed along any and all meridional sections, which, collectively, outlined a shallow zone of low-salinity waters under the Aquarius SSS front. In light that convergence is a primary process in forming a front, this shallow zone may well represent a low-salinity convergence zone (LSCZ).

### 3.3. Seasonal Migration of the Low-Salinity Water and its Relation to the ITCZ Rainfall

The ITCZ rainfall is an apparent source of the low-salinity waters. The ITCZ is known to migrate meridionally with seasons, reaching the northernmost latitude during boreal summer, and moving back to near the equatorial position during boreal winter [*Xie and Arkin*, 1997]. The low-salinity cells along the four selected

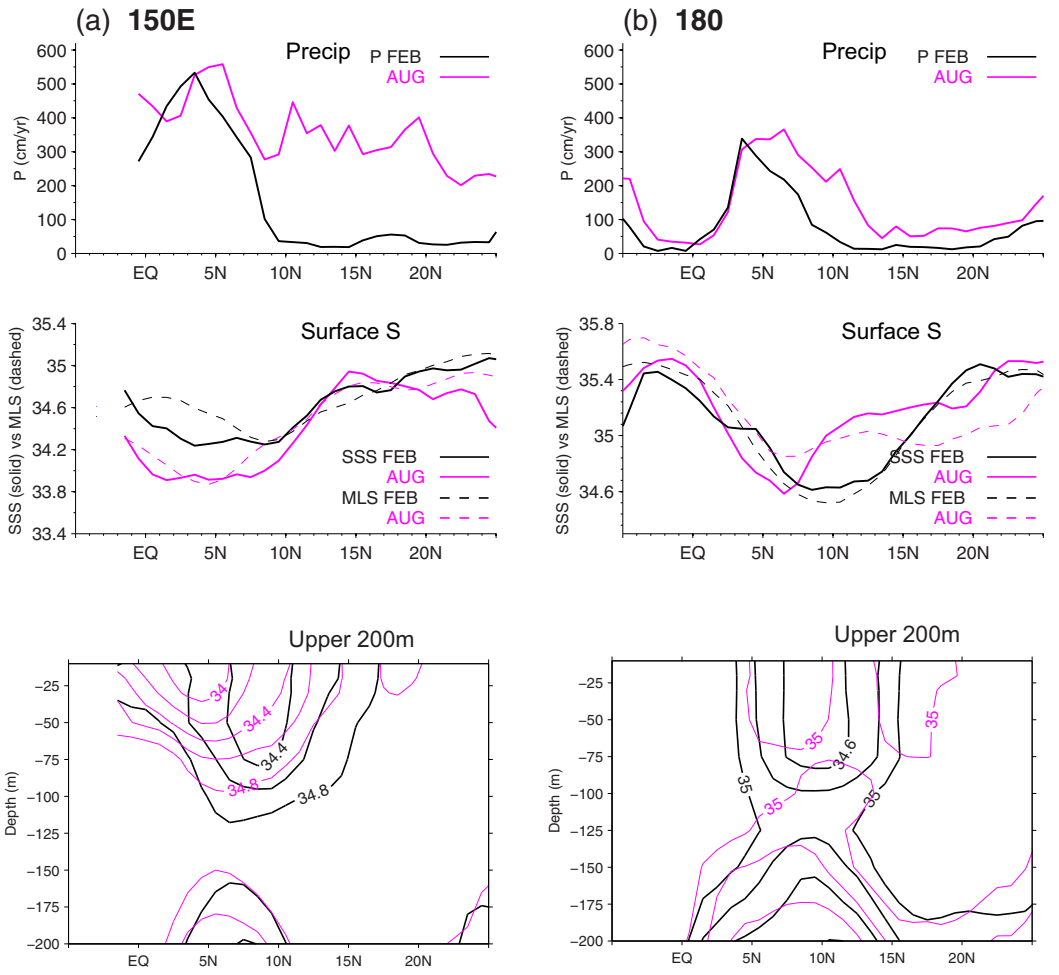


**Figure 2.** Precipitation (top plots), surface salinity (mid plots) from Aquarius SSS (solid) and Argo MLS (dashed)), and salinity subsurface structure (bottom plots) at four meridional sections along (a) 150°E, (b) 180, (c) 140°W, and (d) 110°W in February (black) and August (magenta).

meridional sections all exhibited a marked latitudinal migration with seasons. The dependence of the seasonal movement of the low-salinity cells on the seasonal migration of the ITCZ rainfall was examined using the two contrasting months of February and August (Figures 2a–2d). To check on the consistency of the salinity signals between the surface and the subsurface, the plot of the Aquarius SSS and the Argo MLS was included at each section along with the plots of the ITCZ rainfall *P* and the Argo salinity structure in the upper 200 m. The seasonal change in the ITCZ rainfall is evident, with *P* being stronger and displaced more northward in August than in February (Figures 2a–2d, top plots). The seasonal change was particularly pronounced at 140°W, where the maximum rainfall (hereafter *Pmax*) in August was more than doubled than that in February and the *Pmax* location in the former was about 4° northward from its position in the latter.

Seasonal movement in the low-salinity cores was captured by both Aquarius SSS and Argo MLS observations (Figures 2a–2d, middle plots). Although the fine details between the Argo MLS and the Aquarius SSS did not exactly agree, due likely to the differences in the measurement depth and sampling resolutions, the two sets of surface salinity observations were consistent in depicting the seasonal movement and magnitude variations of the salinity minima (i.e., the *Smin* and MLS minima). Surprisingly, when compared to the seasonal movement of *Pmax*, the direction of the displacement in *Smin* (and the MLS minima) was opposite to that of *Pmax*. The *Smin* location in August was displaced *southward* to its location in February, contrary to the *Pmax* location in August that was displaced *northward* to its location in February. For instance, at 140°W (Figure 2c), the *Smin* moved from 10°N in August to 14°N in February, whereas the *Pmax* migrated from 10°N in August to 6°N in February. Despite their opposing meridional seasonal migration, the

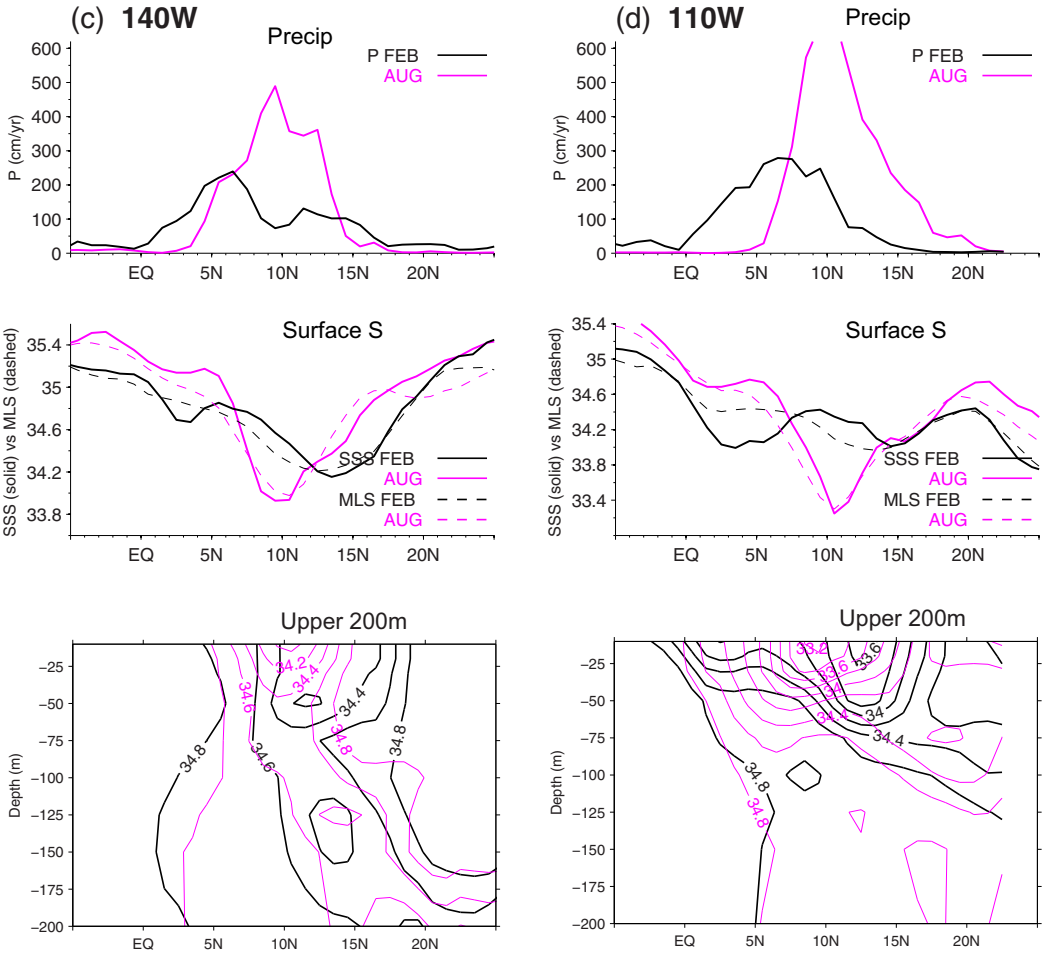


**Figure 2.** (Continued).

locations of the *Pmax* and *Smin* were not completely independent from each other. The two locations were aligned closely together in August even though they were apart in February. The location difference between *Pmax* and *Smin* in February stood as a key feature in characterizing the seasonal relationship between the precipitation and the low-salinity surface waters.

The Argo subsurface salinity sections (Figures 2a–2d, bottom plots) corroborated the evidence from the Aquarius SSS that the core of the near-surface low-salinity cell was aligned directly under the *Pmax* in August, but positioned about 5° north of the *Pmax* in February. Additionally, the low-salinity cell was fresher and deeper in August than in February even though the change of the magnitude of *Pmax* between the two months was not as large along some sections (e.g. 150°E). The evidence seemed to imply that the ITCZ precipitation may not be the only forcing mechanism for controlling the generation and movement of the low-salinity front, though rain was the apparent source of the surface low-salinity waters.

### 3.4. A Basin-Scale Perspective

To characterize the seasonal migration of the surface low-salinity waters and its relationship to the ITCZ precipitation over the entire basin, the standard deviations (STD) of the monthly-mean Aquarius SSS and TRMM precipitation were constructed (Figures 3a and 3b). The locations of *Smin* and *Pmax* were superimposed. The *Smin* location in August coincided with the location of the large seasonal STD of SSS. Similarly, the *Pmax* location in August coincided with the location of the large seasonal STD of *P*. Nevertheless, the seasonal movement of the low SSS showed a marked difference from that of the ITCZ rain band.

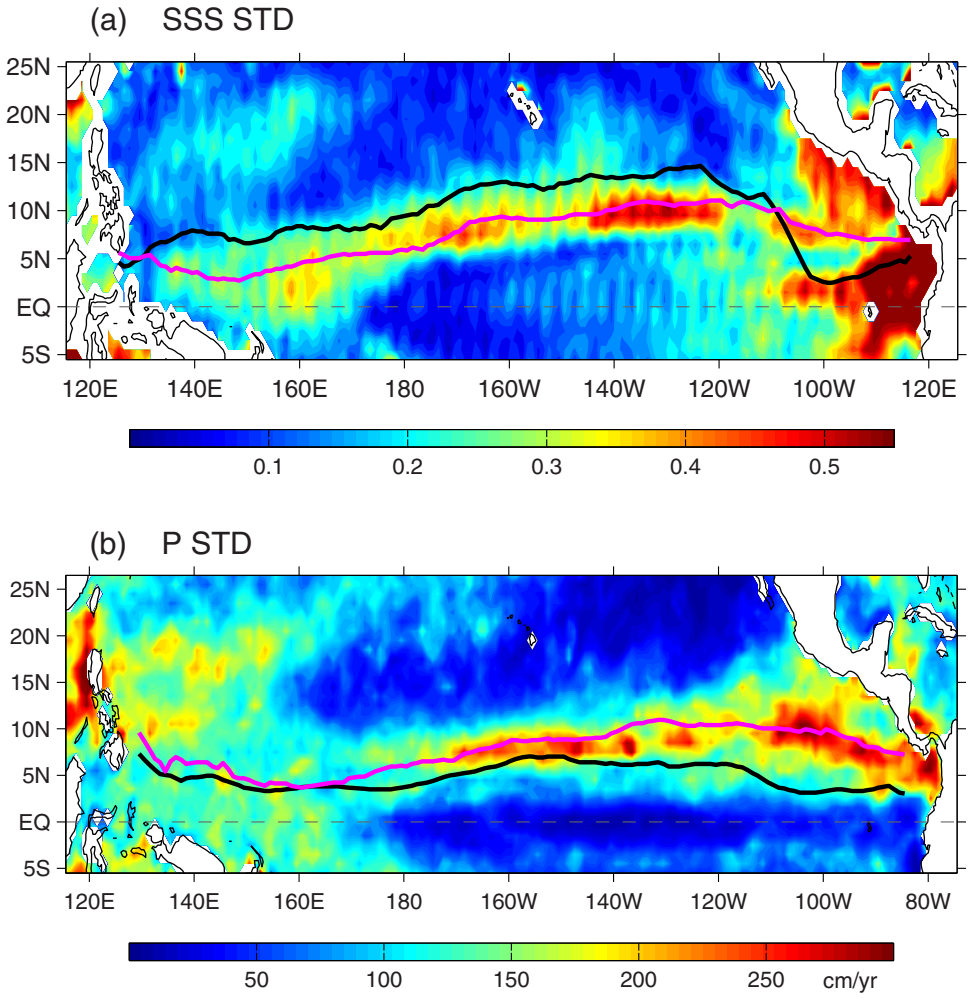


**Figure 3.** (a) Standard deviation (STD) of Aquarius SSS with locations of *Smin* in February (black) and August (magenta) superimposed, and (b) STD of precipitation with locations of *Pmax* in February (black) and August (magenta) superimposed.

The differences in seasonal characteristics between the low SSS zone and the ITCZ rainfall band can be generalized by three features. First, the large magnitudes of STD SSS did not collocate with the large magnitudes of STD *P*. Pronounced seasonal variances of the ITCZ rainfall, with STD exceeding 250 cm/yr, were located in the central and eastern Pacific, whereas the maximal SSS STD ($>$0.4) were located in the east central Pacific (between 150 and 120°W) and the far eastern fresh water pool (east of 110°W). Second, the low SSS zone moved northward from August to February, during which the ITCZ rain band migrated southward. While the seasonal change in the ITCZ location was in line with the conventional description that the ITCZ follows the sun and moves north in boreal summer and south in boreal winter, the seasonal movement of the low SSS zone was not conventional. Last, the *Smin* location in the eastern Pacific moved in the same direction as the seasonal migration of the local rainfall, opposite to the scenario in the western and central Pacific. The change in the location relationship between *Smin* and *Pmax* on the two sides of 110°W may indicate a change of dominant forcing in controlling the seasonal salinity variability in the eastern and western/central Pacific.

### 3.4.1. The Western and Central Tropical Pacific

The time-latitude evolution of the monthly-mean SSS and P at the four meridional sections (Figures 4a and 4b) was analyzed to assess how their relationship has changed through a full seasonal cycle. One marked feature at all SSS sections (Figure 4a) was the northward march of low SSSs starting in the boreal spring season. For instance, the low-salinity signals at the sections along 140°W and 110°W started around March from the near-equatorial latitudes of 2–3°N; they moved progressively northward in the following months,

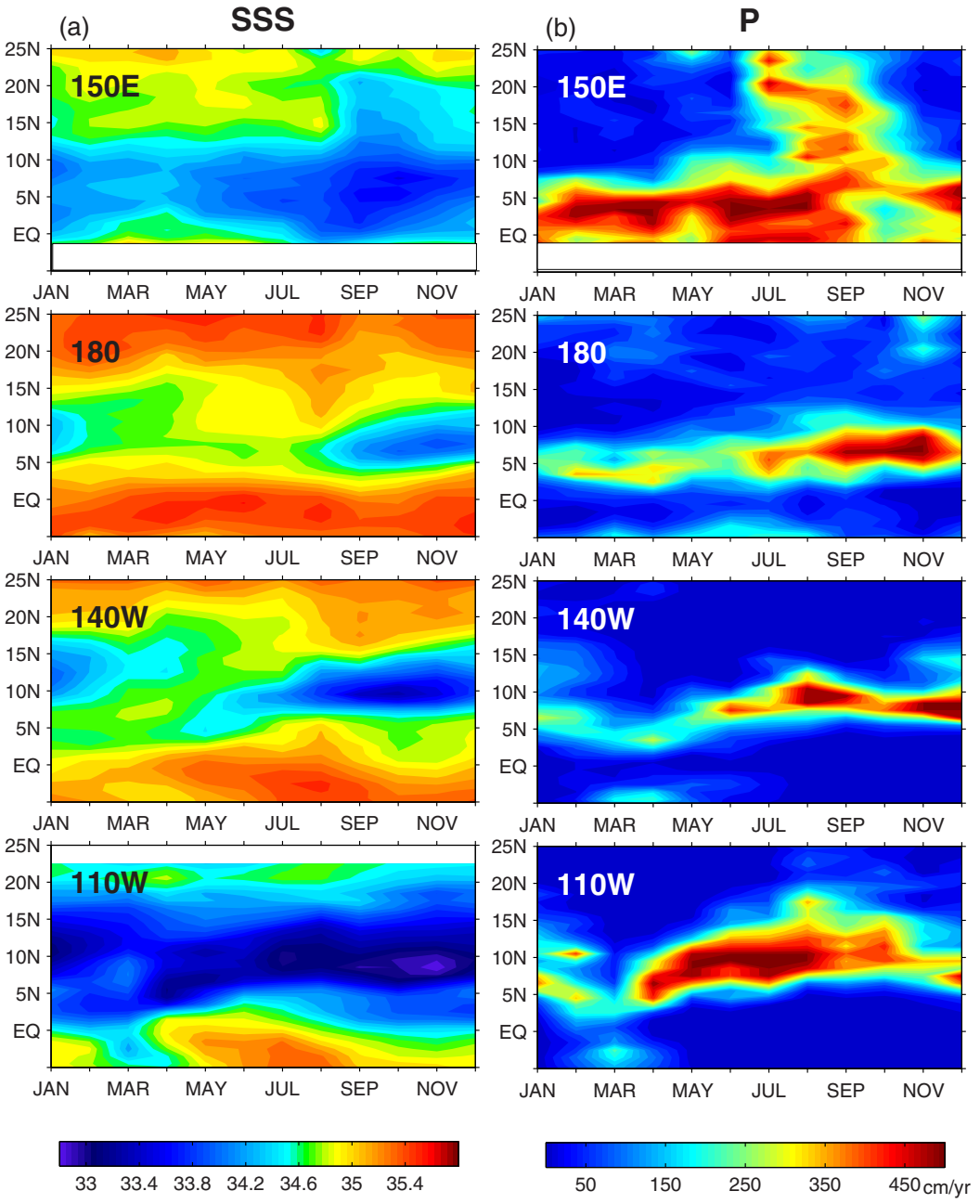


**Figure 4.** Seasonal evolution of (a) Aquarius SSS and (b) precipitation at four meridional sections along 150°E, 180, 140°W, and 110°W (from top to bottom).

reaching the latitude of ~ 15°N in February of the next year. The northward displacement of the low-salinity signals at the section along the dateline had an onset in May and persists until the next spring. Compared to the other sections, the low-salinity signals at the section along 150°E had only a slight northward movement and a weak seasonal cycle.

A northward propagation of heavy rainfall was seen at all four sections (Figure 4b), but it lasted only half of the year, from boreal spring to fall. The heavy rain band moved equatorward in the following months and was located closest to the equator in boreal spring. Evidently, the north-south displacement of the heavy rain band was the major feature of the seasonal cycle of *P*. The seasonal cycle of low SSSs did not follow this pattern; instead, it was noted by a monotonic northward displacement starting from the near-equatorial latitudes in the spring, the time that the rainfall started to intensity. Nevertheless, the northward

progression of low SSSs from boreal spring to summer was in tandem with the movement of the ITCZ rain band. For the other half of the seasonal cycle from boreal fall to winter, the movement of low SSSs decoupled from the movement of *P* cycle in a way that the rain band moved toward the equator while the low SSSs continued its northward excursion. The continuing northward shift of the low SSSs must have been driven by processes other than the surface freshwater flux.

#### 3.4.2. The Eastern Tropical Pacific Fresh Pool

East of 120°W, the open-ocean SSS front (Figures 1a and 1b) veered southward and, at near 105°W, merged with an equatorial SSS front that was centered slightly north of the equator between the coast of South America and 120°W. Meanwhile, a few short-scale localized SSS fronts were also present, the most noted of which was the one located around 7–8°N near the coast of Central America with a westward extension of about 15°. These two local SSS fronts are a broad outline of three major water masses contributing to surface water properties in the region. The equatorial SSS front reflects the merging of the salty South Pacific waters that are produced by the equatorial cold tongue with the fresher surface waters that are generated by the ITCZ rains [*Fiedler and Talley*, 2006; *Kessler*, 2006]. The short-scale front near the coast of Central America is the boundary between a fresh pool induced by monsoon rains and river runoff [*Fiedler and Talley*, 2006; *Alory et al*., 2012] and the fresh surface waters produced directly by the ITCZ rain. It has been known that the northern edge of the equatorial cold tongue, where the South Pacific water meets with the ITCZ-induced fresher surface water, produces pronounced SSS signature of the Tropical Instability Waves (TIWs) [e.g., *Lee et al*., 2012]. TIWs are westward propagating, planetary-scale waves, with 1000–2000 km wavelengths and 20–40 day periods [e.g., *Legeckis*, 1977]. They are generated by the meridional and vertical shear of the equatorial current systems [e.g., *Philander*, 1978]. However, detailed spatial and temporal distributions of the TIWs cannot be fully resolved in the present study due to our focus on the seasonal timescales.

The subsurface salinity structures at the meridional sections along 100°W, 95°W, and 90°W (Figure 5) provided a direct view on the latitudinal distributions of the three major water masses: the salty South Atlantic waters south of the equator, the ITCZ-induced fresher surface waters between 2–10°N, and the coastal fresher surface waters north of 10°N. It is worth noting that even though the two fresher water masses showed a similar salinity, they were associated with different low-salinity cores and were easily recognizable from Figure 5. These three water masses had substantial seasonal variances within their own latitudinal regimes (Figure 3a).

Compared to the SSS pattern and variability west of 120°W, the SSS in the eastern tropical Pacific fresh pool had more complex spatial and temporal features because of the influence of not only the ITCZ rainfall but also river runoff from Central America. The seasonal dynamics of the freshest water pool (SSS $<33$) in the far eastern tropical Pacific between the Panama's west coast and 95°W is presented in *Alory et al*., [2012]. The study provides a detailed analysis of the governance of the ITCZ rainfall on the SSS balance at different seasons [*Donguy and Hénin*, 1980; *Fiedler and Talley*, 2006] and the important role of advection and entrainment processes in the SSS variability in the coastal region [*Bingham et al*., 2010]. The two strong SSS fronts at the southern and northern edges of the freshest water pool, which are the fronts that bound the three major water masses in the region, are also discussed.

Here the evidence that the *Smin* location followed the ITCZ *Pmax* location east of 110°W (Figures 3a and 3b) corroborated with the existing literature [e.g., *Donguy and Hénin*, 1980; *Fiedler and Talley*, 2006; *Alory et al*., 2012] that rainfall is a more direct and controlling forcing for seasonal SSS cycle in the eastern tropical Pacific fresh pool. The SSS-rain connection found in the eastern fresh pool was clearly different from that in the western and central Pacific.

## 4. Mechanisms

### 4.1. Quantifying the Contributions of the Surface Freshwater Forcing and Ocean Processes

The MLS budget analysis was used to diagnose the relative roles of the surface E-P forcing versus ocean advections in seasonal surface salinity variability. By decomposing each variable into an annual mean and the departure from the mean and neglecting the contributions from the mean products of anomalies, the equation for the MLS variability can be written as [[*Mignot and Frankignoul*, 2003; *Yu*, 2011]

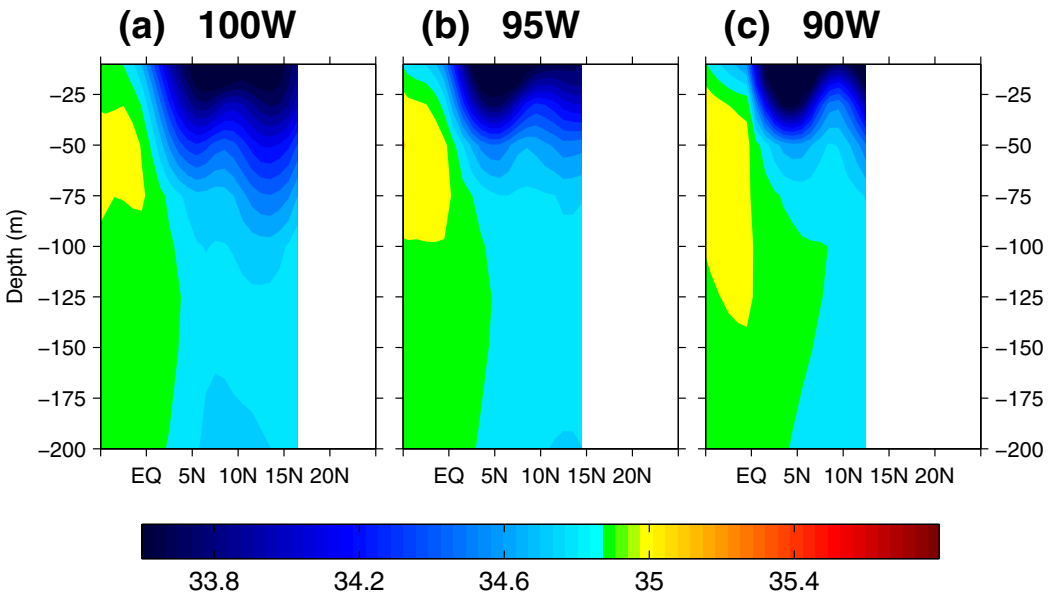


**Figure 5.** Mean salinity vertical structure in the upper 200m at three meridional sections in the eastern Pacific along (a) 100°W, (b) 95°W, and (e) 90°W.

$$\frac{\partial S'}{\partial t} \approx \frac{S_0\left(E'-P'\right)}{\bar{h}} - \bar{\mathbf{U}} \cdot \nabla S' - \mathbf{U}' \cdot \nabla \bar{S} - \frac{\left(\Gamma(w_e)(S-S_b)\right)'}{\bar{h}} + \kappa \nabla^2 S' \tag{1}$$

where an overbar denotes the mean and a prime denotes the departure from the mean, $S$ the MLS, $S_0$ the mean surface salinity, $E$ evaporation, $P$ precipitation, $h$ the mixed-layer depth, $\boldsymbol{U}$ the horizontal transport in the mixed layer, $w_e$ is the entrainment velocity at depth $z=h$, $S_b$ the salinity chosen as the salinity 20 m below the mixed layer depth $h$, $\Gamma$ the Heaviside function, and $\kappa$ the horizontal mixing coefficient set to 500 $ms^{-2}$. The Heaviside function $\Gamma$ is introduced to treat the entrainment and detrainment separately. The entrainment of subsurface stratified water affects the MLS, whereas the detrainment of the mixed layer water to the subsurface does not change the MLS [*Kraus and Turner*, 1967].

The horizontal transport $\boldsymbol{U}$ in equation (1) includes two components, namely, the wind-driven Ekman component $\boldsymbol{U}_{EK}$ and the geostrophic component $\boldsymbol{U}_g$, and can be expressed as:

$$\boldsymbol{U} = \boldsymbol{U}_{EK} + \boldsymbol{U}_g = \frac{\tau \times \boldsymbol{k}}{\rho f} + \frac{hg\nabla\eta \times \boldsymbol{k}}{f} \tag{2}$$

where $\tau$ denotes wind stress, $g$ is the gravity acceleration, $f$ the Coriolis frequency, and $\eta$ the sea surface elevation.

The entrainment velocity $w_e$ in equation (1) consists of vertical Ekman velocity $w_{EK}$ and the $h$ tendency:

$$w_e = w_{EK} + \left(\frac{\partial h}{\partial t} + \nabla \cdot h\boldsymbol{U}\right) = \frac{\nabla \times \boldsymbol{\tau}}{\rho f} + \left(\frac{\partial h}{\partial t} + \nabla \cdot h\boldsymbol{U}\right)$$

The Ekman vertical velocity $w_{EK}$ corresponds to the upwelling/downwelling generated by the convergence/divergence of the horizontal Ekman transport. The $h$ tendency term represents the integrated effects of wind, surface buoyancy flux, and turbulent dissipation on the change of the mixed-layer depth [*Niiler and Kraus*, 1977].

Substituting equation (2) into equation (1) yields the following MLS equation:

$$\frac{\partial S'}{\partial t} \approx \frac{S_0\left(E'-P'\right)}{\bar{h}} - \bar{\mathbf{U}}_{\boldsymbol{EK}} \cdot \nabla S' - \mathbf{U}'_{\boldsymbol{EK}} \cdot \nabla \bar{S} - \bar{\mathbf{U}}_{\boldsymbol{g}} \cdot \nabla S' - \mathbf{U}'_{\boldsymbol{g}} \cdot \nabla \bar{S} - \frac{\left(\Gamma(w_e)(S-S_b)\right)'}{\bar{h}} + \kappa \nabla^2 S' \tag{3}$$

The left-hand side denotes the rate of change of the MLS (or the SSS tendency), while on the right-hand side, the first term denotes the effective surface E-P forcing, the second term is the advection of the MLS by

mean Ekman currents, the third is the advection of the MLS by anomalous Ekman currents, the fourth term is the advection of the MLS by mean geostrophic currents, the fifth term is the advection of the MLS by anomalous geostrophic currents, the sixth term is the entrainment/detrainment of the MLS through the base of the mixed layer, and the last term represents horizontal mixing and is usually small in the tropical oceans.

*Yu* [2011] implemented an approach to differentiate the importance of the terms on the right-hand side of equation (3) based on the magnitudes of their covariance contributions to the term on the left-hand side. The convariance between each contributing term and the change of the MLS was computed individually. At each grid point, the convariances from all the contributing terms were ranked according to the magnitude of the covariances. The order of the ranking defines the relative importance of each term to the change of the MLS, and the top ranked terms are the dominant processes. This approach was applied here to isolate the key processes in the region of study. The Aquarius SSS and the Argo MLS were used, respectively, in the computation to determine the dependence of the constructed forcing regime on the salinity data set in use.

The regime maps of the leading term thus obtained (Figures 6a and 6b) suggested that the two data sets were highly consistent in delineating the regime of key processes, albeit the Aquarius SSS produced a noisier pattern. The two maps all showed that the salinity advection by mean Ekman currents was the leading forcing for surface salinity variability in the western and central basin (between 160°E and 120°W), whereas the surface freshwater forcing dominated the western Pacific fresh pool (west of 160°E) and the eastern Pacific fresh pool (east of 120°W). Despite the similarity, there was a noted difference between the two patterns in area around 10°N between 170°E and 150°W, where the Argo-based pattern (Figure 6b) indicated that the leading forcing was the surface freshwater forcing, not the Ekman advection that was seen in the Aquarius-based pattern (Figure 6a). Our analysis indicated that the cause of the difference was the pattern difference in the two salinity data sets in the boreal summer. Aquarius SSS produced a sharp SSS front that was aligned better the Ekman salt convergence. By comparison, Argo MLS had a broad and weak salinity front that agreed more with the broad ITCZ rain band. The plot of the Argo MLS versus Aquarius SSS along 180 (Figure 2b, middle plot) provided a comparison of the two data sets in August (solid and dashed magenta lines). The coarse spatial resolution of Argo might be the cause of the broad salinity front, as Argo has a nominal spatial resolution of 3° [*Riser et al*., 2008].

The map of the leading term produced here was in broad agreement with that of *Yu* [2011, Figure 9], except that the regime of the freshwater forcing in this study covers less area in the central tropical Pacific, particularly missing the ITCZ rain band. One likely cause was the length of data record and potential influence of interannual variability. The present analysis focused on the seasonal cycle derived from the 2 year Aquarius observing period from September 2011 to August 2013, whereas the study of *Yu* [2011] utilized the salinity climatology of the World Ocean Atlas (WOA) [*Antonov* et al., 2010] that is compiled from in situ measurements over the past 50 or more years. It is possible that the Aquarius years were not a climatological condition so that one forcing was particularly favored, leading to abnormally larger contribution to the seasonal variability. Nonetheless, the regime maps for the second leading term produced by both present and previous studies (not shown) agreed with each other on that the freshwater and the mean Ekman advection were the alternative primary mechanism for the salinity variability under the ITCZ. These two processes compete against each other in governing the SSS seasonal variances in the region.

### 4.2. Roles of the Ekman Advection and the Surface Freshwater Forcing

The spatial distributions of the covariance contributions from the respective E-P flux and the mean Ekman advection to the change of SSS (Figures 7a and 7b) were shown to help delineate how the two terms, namely, the E-P flux and the mean Ekman advection, controlled the SSS seasonal variability. While the mean Ekman advection was a clear leading forcing in the broad central basin between 160°E and 120°W, the E-P flux dominated in the three regions, the western tropical Pacific fresh pool, the eastern tropical Pacific fresh pool, and a narrow zonal band along 10°N across the central basin. They each were responsible for at least 60% of the observed SSS variances in their respective dominant regimes. One interesting revelation was that, though both processes were present in the central basin, the influence of the E-P flux was limited to a narrow and zonally oriented band, whereas the influence of the mean Ekman advection covered a wider

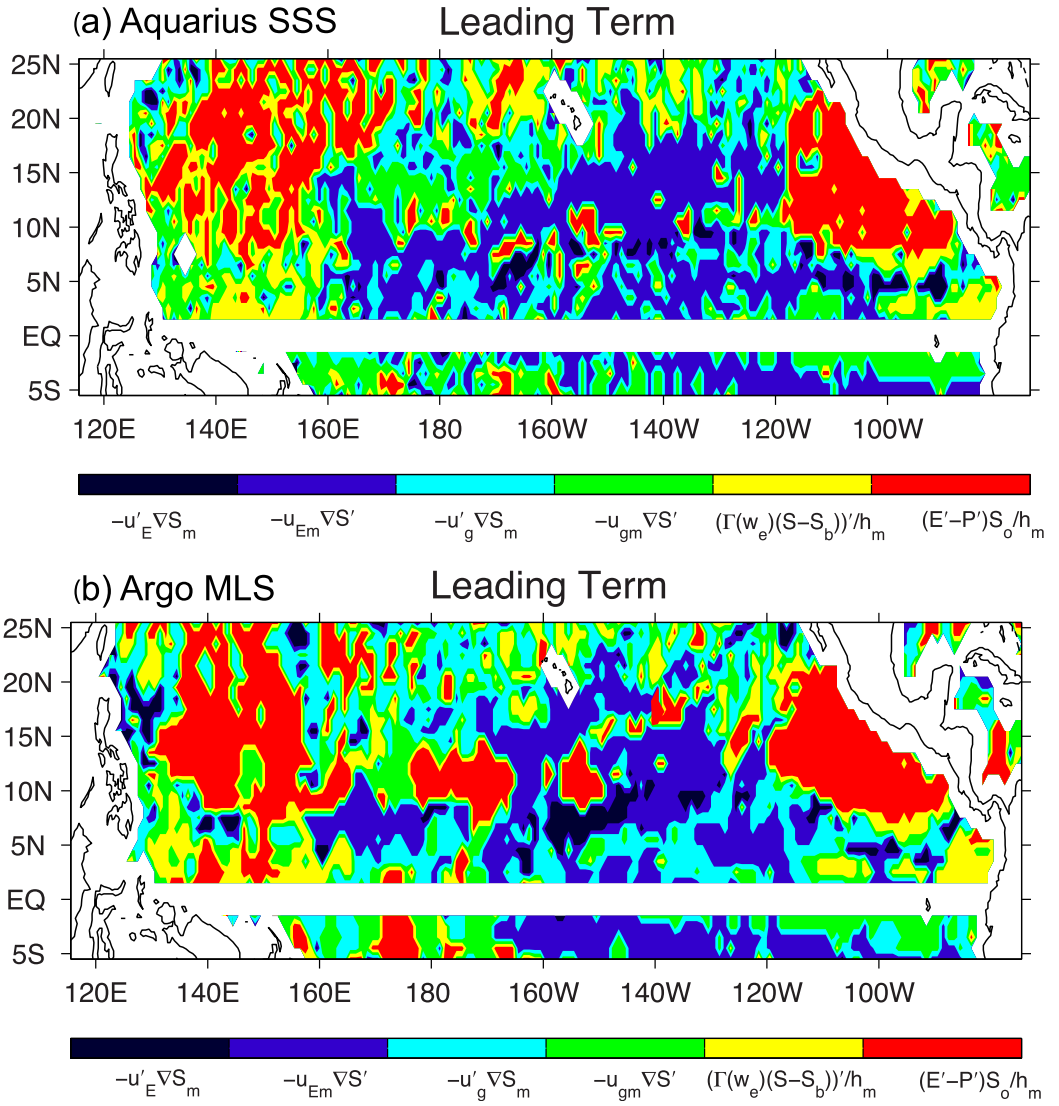


**Figure 6.** Regime map of the leading forcing for seasonal variability of near-surface salinity computed from (a) Aquarius SSS and (b) Argo mixed-layer salinity. The six processes used in the computation include anomalous Ekman salt advection (dark blue), mean Ekman salt advection (blue), anomalous geostrophic salt advection (cyan), mean geostrophic salt advection (green), vertical salt transport by upwelling (yellow), and the E-P forcing (red).

area that was aligned in a southwest-northeast direction. A similar northeastward tilt was noted in the SSS STD across the central basin (Figure 3a).

The seasonal cycles of the SSS tendency, the two leading forcing, and the combined effect of the two forcings were constructed at the four meridional sections along 150°E, 180°, 140°W, and 110°W (Figures 8a–8d). The northward progression of the SSS seasonal anomalies was featured at all sections, albeit with various phase speeds. For instance, at the section along 150°E (Figure 8a, top plot), the northward propagation of the SSS signals were present between 5°S and 8°N, with a negative SSS (freshening) tendency between May and August and a positive SSS (salinification) tendency between July and December. Along 140°W (Figure 8c), the negative tendency anomaly started from near 2°N in March and propagated to near 15°N in November.

The northward displacement of the SSS tendency anomalies along 180 and 140°W (Figures 8b and 8c) was controlled more by the Ekman salt transport and less by the E-P forcing. Between April and September, the E-P anomalies indicated a slight northward shift, and the movement was in phase with the effect of the Ekman advection. Between October and December, the E-P anomalies propagated equatorward, opposite

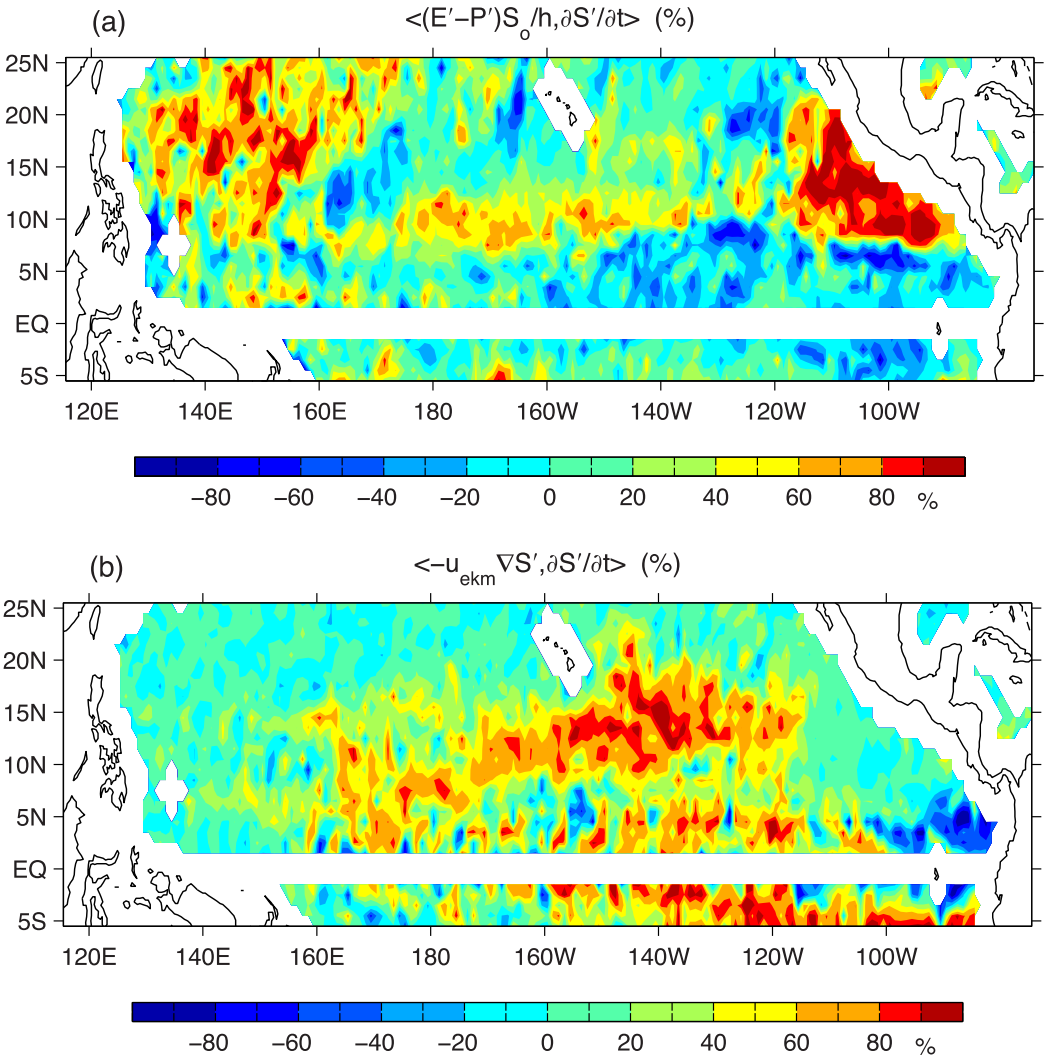


**Figure 7.** Normalized covariance (a) between the E-P forcing and the rate of change in SSS ($\partial S'/\partial t$), and (b) between mean Ekman salt advection and $\partial S'/\partial t$. Aquarius SSS is used in the computation.

to the direction of the Ekman advection. Along 110°W (Figure 8d), the E-P flux was more dominant. The range of the meridional extent of the SSS tendency anomalies showed a good agreement with that of the freshwater forcing, extending from near the equator all the way to 20°N. By comparison, the mean Ekman salt transport anomalies were confined mostly within 10°N. Along 150°E (Figure 8a), the freshwater forcing showed a slight dominance over the mean advection in contributing to SSS tendency anomalies, but the effects of both forcings were weak. The evidence in Figures 8a–8d suggested that the northward propagation of the SSS tendency anomalies in the central basin was governed primarily by the northward Ekman advection, and that the SSS tendency anomalies in the eastern Pacific fresh pool was more a local response to the change of the freshwater flux associated with the ITCZ seasonal migration.

### 4.3. Ekman Convergence and the Location of the Smin

The Ekman currents, which are distributed nonuniformly throughout the basin, drive the surface waters to converge toward some places and diverge from other places. Convergence pushes the surface waters downward, whereas divergence upwells the subsurface waters. Here we show that the convergence/divergence pattern of the Ekman salt transport had a deciding role in determining the location of the *Smin*.

The superimposition of the locations of *Smin* and *Pmax* of onto the Ekman advection of SSS anomalies in February and August (Figures 9a and 9b) revealed an important relationship, that is, the location of the *Smin* was always on the northern edge of the convergence (positive) anomalies of the Ekman advection, no

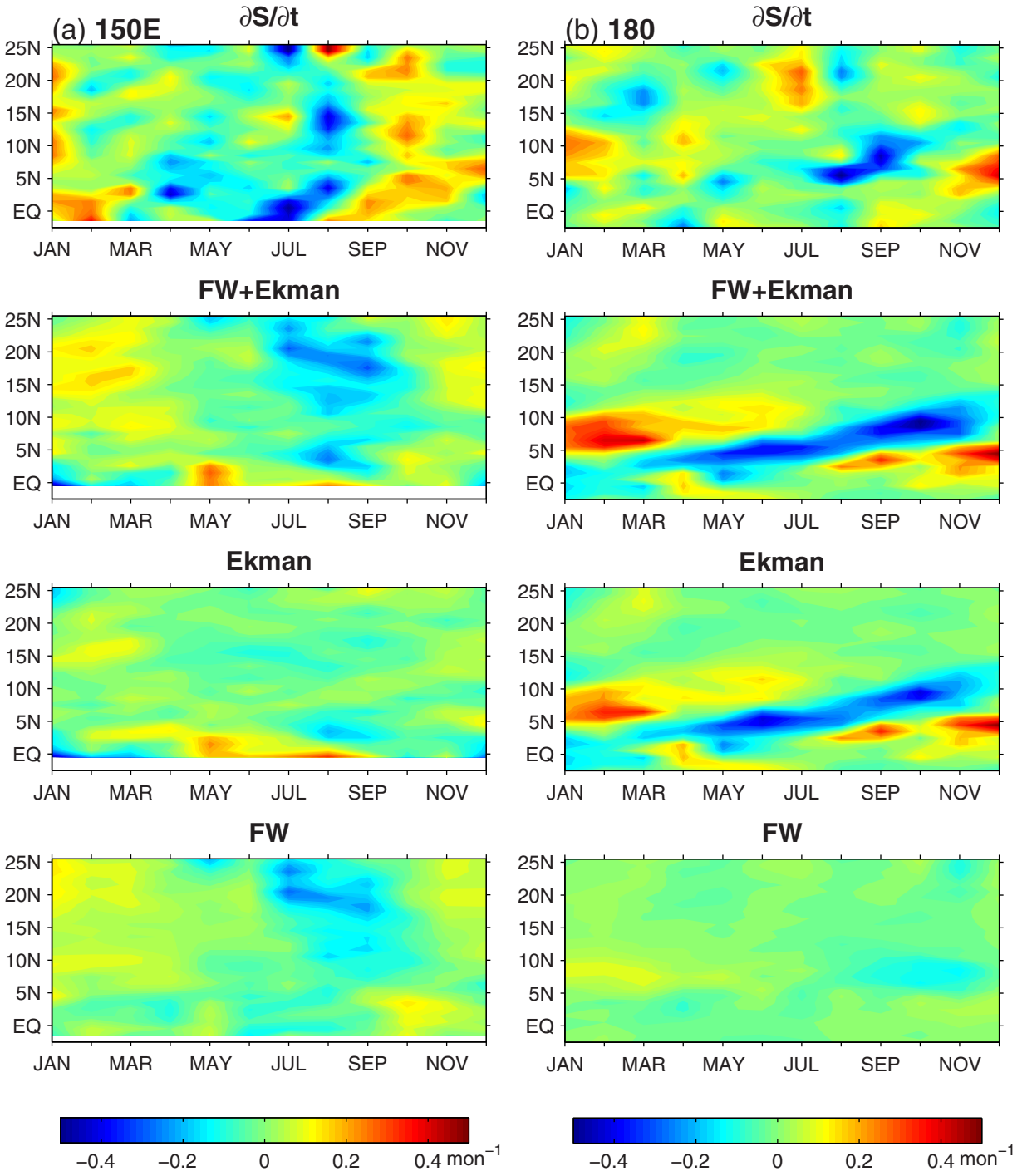


**Figure 8.** Seasonal evolution of (from top to bottom) the rate of change in SSS ($\partial S'/\partial t$), the E-P forcing plus mean Ekman salt advection, mean Ekman salt advection, and the E-P forcing along (a) 150°E, (b) 180, (c) 140°W, and (d) 110°W.

matter whether it was February or August. This connection firmly established the Ekman convergence as the genesis of the low-salinity convergence zone beneath the ITCZ. Given that the location of the *Smin* was also on the northern edge of the SSS front (Figure 1a), the SSS front was intrinsically a manifestation of the Ekman convergence of low-salinity surface waters.

On the other hand, the low SSS showed no fixed relationship with the *Pmax*. The superimposition of the locations of *Smin* and *Pmax* onto the E-P anomalies in February and August (Figures 9c and 9d) indicated

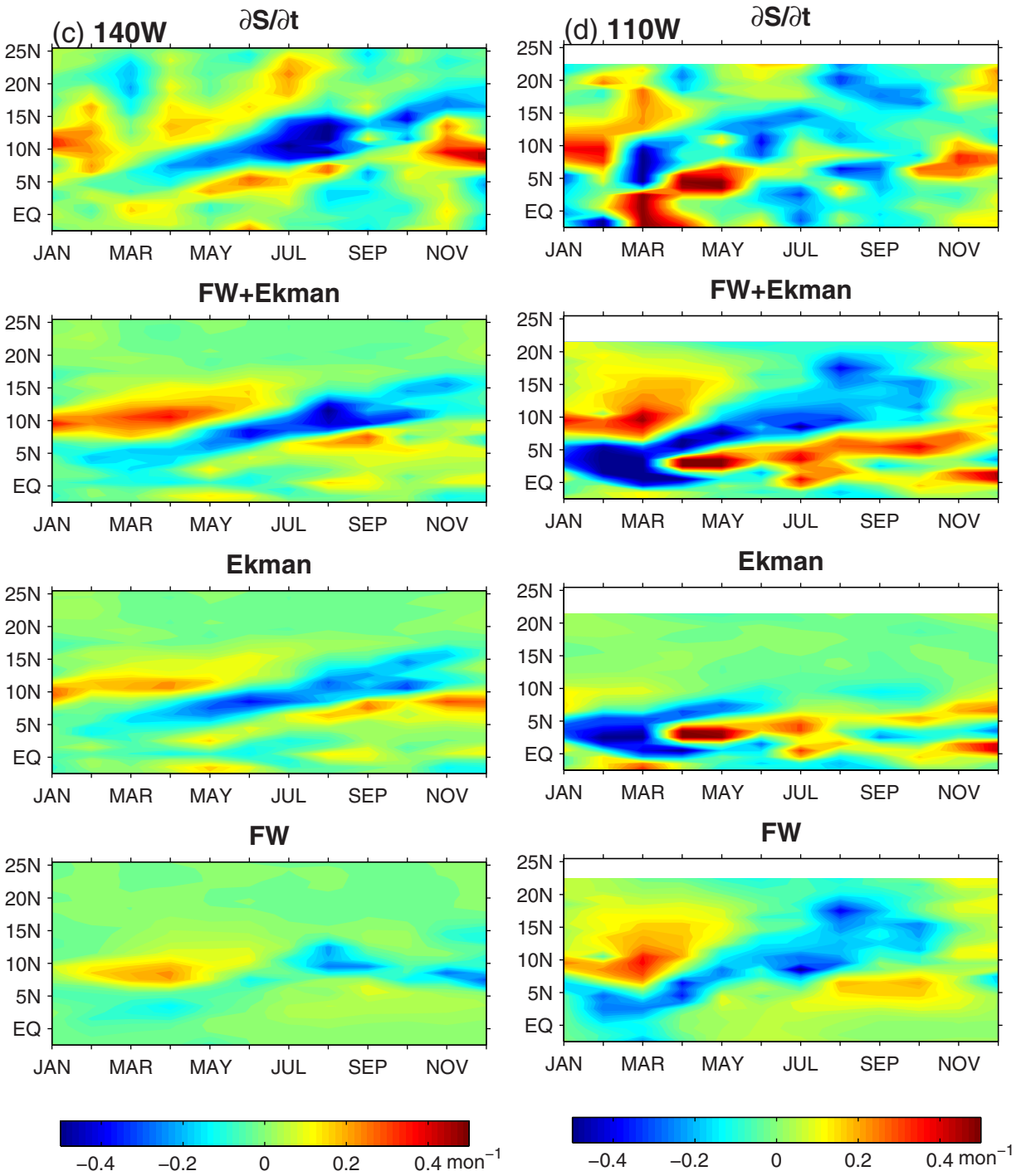


**Figure 8.** (Continued)

that *Smin* could be aligned entirely with the *Pmax* in August, and it could also be displaced 5–8° north of the *Pmax* in February. The changing location relationship between the *Smin* and the *Pmax* reflected the fact that the ITCZ rains were the source of the low-salinity surface waters, but the Ekman processes determined where the fresher surface waters were advected and converged into the subsurface to form a low-salinity convergence zone. In February, the *Pmax* were positioned within 5° of the equator and the *Smin* were located between 5–12°N—the separation of 5–8 latitude degrees between the two was

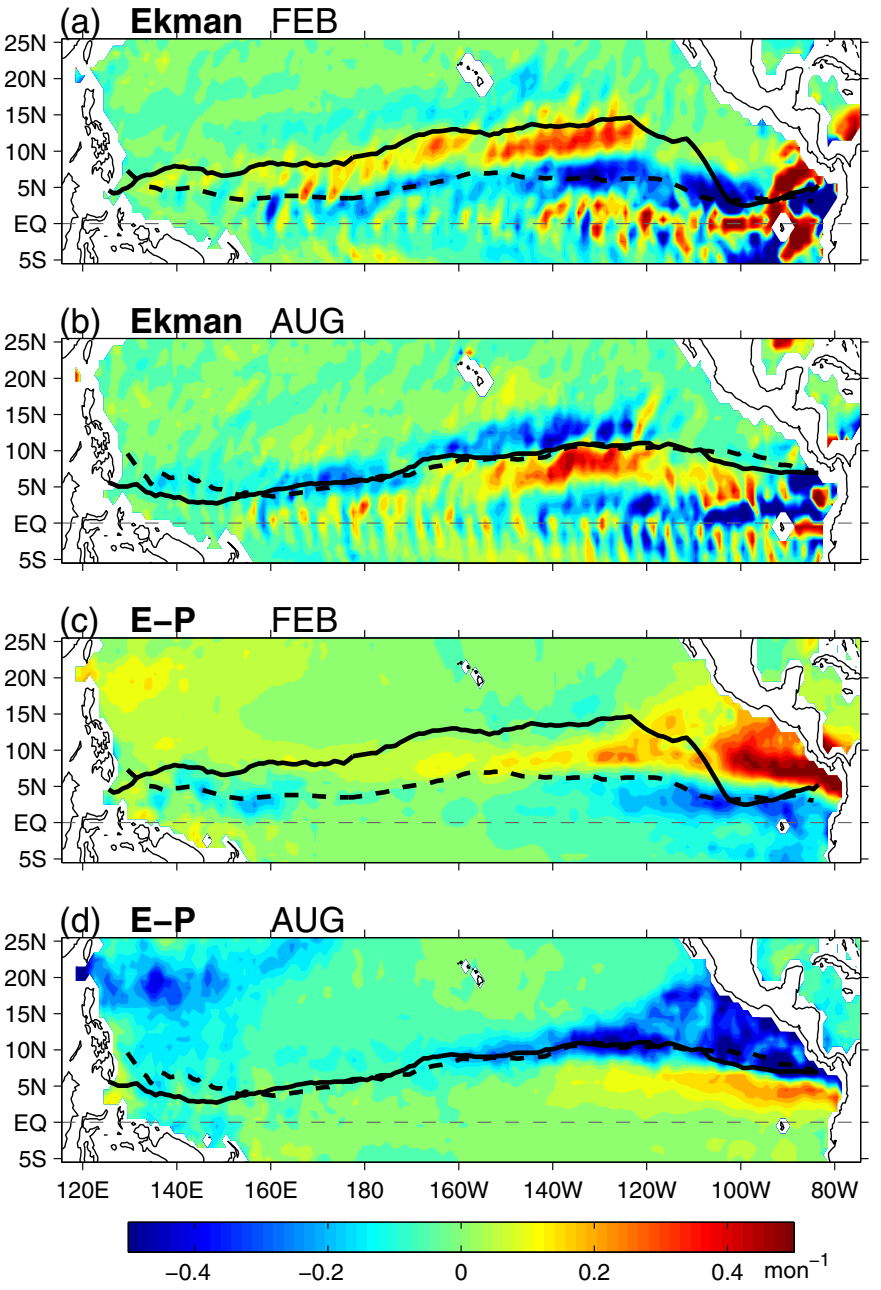


**Figure 9.** Mean Ekman salt advection ($-\bar{U}_{EK} \cdot \nabla S'$) in (a) February and (b) August, along with the E-P forcing ($(E' - P')S_0/\bar{h}$)) in (c) February and (d) August. The two superimposed lines denoted the locations of the *Smin* (black solid) and *Pmax* (black-dashed) for the respective month.

caused by the northward Ekman transport. In August, the heavy rain anomalies coincided with the Ekman convergence (positive) anomalies. Hence, the rain-induced fresh surface waters were formed and converged into the subsurface directly under the ITCZ, giving rise to the collocation between the *Smin* and *Pmax*.

The Ekman processes appeared to have the strongest influence on SSS seasonal variability in the central Pacific between 160°E and 120°W. The zonal averages of *Smin* and *Pmax* locations in this region was constructed for each of the 12 months to examine the change of the relationship through the year (Figure 10). The locations of the *Smin* and *Pmax* had a perfect alignment from August through October, but were separated by as much as 5–6°N apart during January–May.

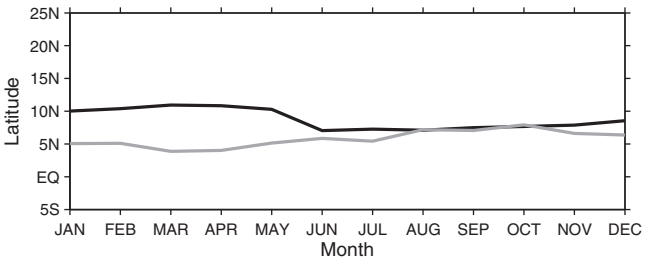


**Figure 10.** Seasonal evolution of the locations of the *Smin* (black) and *Pmax* (gray) averaged in the western and central Pacific between 160°E and 120°W.

## 5. Summary and Conclusions

The Aquarius observations revealed a prominent sea-surface salinity (SSS) front that extended across the tropical Pacific between 2 and 10°N (Figure 1a). By linking to Argo subsurface salinity observations (Figure 1b), the study discovered that the SSS front was not a stand-alone feature; rather, it was a surface manifestation of a shallow low-salinity convergence zone (LSCZ) that existed within 100 m of the upper ocean in the vicinity of the ITCZ (Figures 1c–1f). The structure and seasonal variability of the LSCZ and the mechanisms that generated and maintained the zone were examined in this study by focusing on the 2 year Aquarius observing period from September 2011 to August 2013. A suite of satellite-derived products including MDT, SSH, precipitation, evaporation, and winds was used along with a mixed-layer salinity budget equation to help interpret the salinity frontal features revealed by Aquarius and Argo. Major findings of the study are summarized as follows.

1. The LSCZ was sourced from the ITCZ rainfall, but the seasonal movement of the zone did not follow the seasonal migration of the ITCZ (Figures 2 and 3). This was particularly the case in the western and central Pacific (i.e., west of 120°W). While the ITCZ migrated north in boreal summer and south in boreal winter, the seasonal movement of the low SSS zone was characterized by a monotonic northward displacement starting from the near-equatorial latitudes in the spring, the time that the ITCZ rain band started to intensify and move northward. The study showed that the northward progression of the low SSS zone from the boreal spring to summer was in tandem with the movement of the ITCZ rain band. For the other half of the seasonal cycle from the boreal fall to winter, the movement of the low SSS zone decoupled from the movement of *P* cycle in a way that the rain band moved toward the equator while the low SSSs continued its northward excursion (Figure 4).

2. The leading mechanism that governed the generation and seasonal migration of the LSCZ was the Ekman processes (Figures 6 and 7). The analysis of the ML salinity budget equation showed that the Ekman currents carried the fresh surface waters near the ITCZ latitudes northward, during which the Ekman pumping converged and pushed the fresher surface waters downward to form a shallow low-salinity convergence zone in the upper ocean layer (Figure 8). One revealing relationship was that the location of the *Smin* was always locked to the northern edge of the Ekman convergence, no matter what the season was (Figure 9). This direct connection firmly established the Ekman convergence as the genesis of the low-salinity convergence zone beneath the ITCZ. Since the location of the *Smin* was also located on the northern edge of the SSS front (Figure 1a), the collocation between the SSS front and the Ekman convergence zone not only established the Ekman convergence as the genesis of the LSCZ but also positioned the SST front as a surface manifestation of the LSCZ.

3. Collocations of the *Smin* and *Pmax* were found in August, the time that the Ekman convergence zone was aligned completely with the ITCZ rain band (Figure 9). In February, the *Pmax* were positioned within 5° of the equator and the *Smin* were located between 5 and 12°N—the separation of 5–8° between the two occurred at the time that the Ekman convergence zone was displaced 5–8° north of the ITCZ rain band (Figure 9). The dominant role of the Ekman processes in governing the location relationship between the *Smin* and the *Pmax* was evidenced. Throughout the year, the close alignment between the *Smin* and *Pmax* locations existed from August to October.

4. The seasonal relationship between the *Smin* and *Pmax* differs in the eastern Pacific east of 120°W (Figures 3a and 3b). The seasonal movement of the *Smin* location in the eastern Pacific followed that of the *Pmax* location, unlike the relationship found in the western and central Pacific. The mixed-layer salinity budget analysis showed that the Ekman currents were weak east of 120°W, and the regional SSS seasonal variability responded more directly to local rainfall (Figures 6 and 7).

In summary, the study found that the Aquarius and Argo observations were coherent in revealing the existence of a shallow LSCZ under the SSS front in the tropical Pacific. The LSCZ owed its source to the ITCZ rainfall, but the mechanism of its generation and maintenance on seasonal timescales were dominated by the wind-driven Ekman dynamics, not the surface freshwater flux. The findings of this study bear potentially important implications for the study of the global ocean water cycle and the role of salinity in regional air-sea interaction. The presence of a shallow LSCZ in the vicinity of the ITCZ opens up the possibilities of tracking the ITCZ precipitation variability through observing the low-salinity change within the LSCZ, and using the months between August–October as a test ground to evaluate the freshwater flux estimates derived from the salinity observations against those computed from the conventional bulk flux parameterization. The distinct spatial and seasonal variability of the LSCZ in the ocean and its unique connection with the ITCZ in the atmosphere may be an indication that the LSCZ-ITCZ couplet is an important component of the regional dynamic system.

**Acknowledgments**

The study was supported by the NASA Ocean Salinity Science Team (OSST) under grant NNX12AG93G. Support from the NOAA Office of Climate Observation (OCO) under grant NA09OAR4320129 and NASA Ocean Vector Wind Science Team (OVWST) under grant NNA10AO86G in developing OAFlux evaporation and surface wind stress used in the study is gratefully acknowledged. Dr. Xiangze Jin helped process Aquarius SSS products and assisted in the computation of Figure 6. Ms. Shirley Cabral-McDonald proofread the manuscript. The OAFlux evaporation and wind stress can be downloaded from http://oaflux.whoi.edu. The Aquarius CAP SSS products were from JPL PO.DAAC ftp://podaac.jpl.nasa.gov/allData/aquarius/L2/CAPv2/. The Argo-based gridded salinity and temperature fields were from the JAMSTEC Argo group ftp://ftp2.jamstec.go.jp/pub/argo/MOAA_GPV/Glb_PRS/OI/. The altimeter products were produced by Ssalto/Duacs and distributed by AVISO, with support from Cnes (http://www.aviso.oceanobs.com/duacs/). The mean dynamic ocean topography was from http://apdrc.soest.hawaii.edu/projects/DOT/. The TRMM precipitation 3B43 products were from ftp://disc2.nascom.nasa.gov/data/s4pa/TRMM_L3/TRMM_3B43/.

## References

Adler, R. F., et al. (2003), The Version-2 Global Precipitation Climatology Project (GPCP) monthly precipitation analysis (1979–present), *J. Hydrometeorol.*, *4*, 1147–1167.

Alory, G., C. Maes, T. Delcroix, N. Reul, and S. Illig (2012), Seasonal dynamics of sea surface salinity off Panama: The far eastern Pacific fresh pool, *J. Geophys. Res.*, *117*, C04028, doi:10.1029/2011JC007802.

Antonov, J. I., D. Seidov, T. P. Boyer, R. A. Locarnini, A. V. Mishonov, H. E. Garcia, O. K. Baranova, M. M. Zweng, and D. R. Johnson (2010), World Ocean Atlas 2009, Volume 2: Salinity, in *NOAA Atlas NESDIS 69*, 184 pp., edited by S. Levitus, U.S. Gov. Print. Off., Washington, D. C.

Bingham, F. M., G. R. Foltz, and M. J. McPhaden (2010), Seasonal cycles of surface layer salinity in the Pacific Ocean, *Ocean Sci.*, *6*, 775–787, doi:10.5194/os-6-775-2010.

de Boyer Montégut, C., G. Madec, A. S. Fischer, A. Lazar, and D. Iudicone (2004), Mixed layer depth over the global ocean: An examination of profile data and a profile-based climatology, *J. Geophys. Res.*, *109*, C12003, doi:10.1029/2004JC002378.

Delcroix, T., and C. Henin, (1991), Seasonal and interannual variations of sea-surface salinity in the tropical Pacific ocean, *J. Geophys. Res.*, *96*(C12), 22,135–22,150, doi:10.1029/91JC02124.

Delcroix, T., C. Henin, V. Porte, and P. Arkin (1996), Precipitation and sea surface salinity in the tropical Pacific, *Deep Sea Res., Part 1*, *43*, 1123–1141.

Donguy, J. R., and C. Hénin (1980), Surface conditions in the eastern equatorial Pacific related to the intertropical convergence zone of the winds, *Deep Sea Res., Part A*, *27*, 693–714, doi:10.1016/0198-0149(80)90023-0.

Durack, P. J., and S. E. Wijffels (2010) Fifty-year trends in global ocean salinities and their relationship to broad-scale warming, *J. Clim.*, *23*, 4342–4362, doi:10.1175/2010JCLI3377.1.

Elliott, G. W. (1974), Precipitation Signatures in sea-surface-layer conditions during BOMEX, *J. Phys. Oceanogr.*, *4*, 498–501.

Emery, W. J. (2003), *Water Types and Water Masses, Ocean Circulation*, pp. 1556–1567, Elsevier Sci., Amsterdam, Netherlands.

Fiedler, P. C., and L. D. Talley (2006), Hydrography of the eastern tropical Pacific: A review, *Prog. Oceanogr.*, *69*(2), 143–180, doi:10.1016/j.pocean.2006.03.008.

Font, J., A., Camps, A. Borges, M. Martín-Neira, J. Boutin, N. Reul, Y. H. Kerr, A. Hahne, and S. Mecklenburg (2010), SMOS: The challenging sea surface salinity measurement from space, *Proc. IEEE*, *98*(5), 649–665, doi:10.1109/JPROC.2009.2033096.

Foltz, G. R., and M. J. McPhaden (2008), Seasonal mixed layer salinity balance of the tropical North Atlantic ocean, *J. Geophys. Res.*, *113*, C02013, doi:10.1029/2007JC004178.

Gierach, M. M., J. Vazquez-Cuervo, T. Lee, and V. M. Tsontos (2013), Aquarius and SMOS detect effects of an extreme Mississippi river flooding event in the Gulf of Mexico, *Geophys. Res. Lett.*, *40*, 5188–5193, doi:10.1002/grl.50995.

Grodsky, S., N. Reul, G. Lagerloef, G. Reverdin, J. Carton, B. Chapron, Y. Quilfen, V. Kudryavtsev, and H. Kao (2012), Haline Hurricane Wake in the Amazon/Orinoco Plume: AQUARIUS/SACD and SMOS Observations, *Geophys. Res. Lett.*, *39*(20), L20603, doi:10.1029/2012GL053335.

Grunseich, G., B. Subrahmanyam, and B. Wang (2013), Aquarius salinity observations detect the Madden-Julian oscillation, *Geophys. Res. Lett*, *40*, 5461–5466, doi:10.1002/2013GL058173.

Hénin, C., Y. Du Penhoat, and M. Ioualalen (1998), Observations of sea surface salinity in the western Pacific fresh pool: Large-scale changes in 1992–1995, *J. Geophys. Res.*, *103*(C4), 7523–7536, doi:10.1029/97JC01773.

Huffman, G. J., D. T. Bolvin, E. J. Nelkin, D. B. Wolff, R. F. Adler, G. Gu, Y. Hong, K. P. Bowman, and E. F. Stocker (2007), The TRMM Multisatellite Precipitation Analysis (TMPA): Quasi-global, multiyear, combined-sensor precipitation estimates at fine scales, *J. Hydrometeor.*, *8*, 38–55.

Hosoda, S., T. Ohira, and T. Nakamura (2008), A monthly mean dataset of global oceanic temperature and salinity derived from Argo float observations, *JAMSTEC Rep. Res. Dev.*, *8*, 47–59. [Available at ftp://ftp2.jamstec.go.jp/pub/argo/MOAA_GPV/Glb_PRS/OI/.]

Huang, R. X., and X. Jin (2002), Sea surface elevation and bottom pressure anomalies due to thermohaline forcing. Part I: Isolated perturbations, *J. Phys. Oceanogr.*, *32*, 2131–2150, doi:10.1175/1520-0485.

Johnson, E. S., G. S. E. Lagerloef, J. T. Gunn, and F. Bonjean (2002), Surface salinity advection in the tropical oceans compared with atmospheric freshwater forcing: A trial balance, *J. Geophys. Res.*, *107*(C12), 8014, doi:10.1029/2001JC001122.

Joyce, R. J., J. E. Janowiak, P. A. Arkin, and P. Xie (2004), CMORPH: A method that produces global precipitation estimates from passive microwave and infrared data at high spatial and temporal resolution, *J. Hydrometeor.*, *5*, 487–503.

Kessler, W. S. (2006), The circulation of the eastern tropical Pacific: A review, *Prog. Oceanogr.*, *69*(2–4), 181–217, doi:10.1016/j.pocean.2006.03.009.

Kraus, E. B., and J. S. Turner (1967), A one dimensional model of the seasonal thermocline. II: The general theory and its consequences, *Tellus*, *19*, 98–106.

Lagerloef, G., et al. (2008), The Aquarius/SAC-D Mission: Designed to meet the salinity remote-sensing challenge, *Oceanography*, *21*(1), 68–81doi: 10.5670/oceanog.2008.68.

Lagerloef, G., R. Schmitt, J. Schanze, and H.-Y. Kao (2010), The ocean and the global water cycle, *Oceanography*, *23*(4), 82–93, doi:10.5670/oceanog.2010.07.
Lee, T., G. Lagerloef, M. M. Gierach, H.-Y. Kao, S. Yueh, and K. Dohan (2012), Aquarius reveals salinity structure of tropical instability waves, *Geophys. Res. Lett.*, *39*, L12610, doi:10.1029/2012GL052232.
Legeckis, R., (1977). Long waves in the eastern equatorial Pacific Ocean: A view from a geostationary satellite, *Science 197*(4309), 1179–1181.
Lorbacher, K., S. J. Marsland, J. A. Church, S. M. Griffies, and D. Stammer (2012), Rapid barotropic sea level rise from ice sheet melting, *J. Geophys. Res.*, *117*, C06003, doi:10.1029/2011JC007733.
Lukas, R., and E. Lindstrom (1991), The mixed layer of the western equatorial Pacific Ocean, *J. Geophys. Res.*, *96*(S01), 3343–3357, doi:10.1029/90JC01951.
Maes, C., and T. J. O'Kane (2014), Seasonal variations of the upper ocean salinity stratification in the Tropics, *J. Geophys. Res. Oceans*, *119*, 1706–1722, doi:10.1002/2013JC009366.
Maximenko, N. A., P. Niiler, M.-H. Rio, O. Melnichenko, L. Centurioni, D. Chambers, V. Zlotnicki, and B. Galperin (2009), Mean dynamic topography of the ocean derived from satellite and drifting buoy data using three different techniques, *J. Atmos. Oceanic Technol.*, *26*(9), 1910–1919.
Mignot, J., and C. Frankignoul (2003), On the interannual variability of surface salinity in the Atlantic, *Clim. Dyn.*, *20*, 555–565.
Niiler, P. P., and E. B. Kraus (1977), One-dimensional models, in *Modeling and Prediction of the Upper Layers of the Ocean*, edited by E. B. Kraus, pp. 143–172, Pergamon, N. Y.
Niiler, P. P., N. A. Maximenko, and J. C. McWilliams (2003), Dynamically balanced absolute sea level of the global ocean derived from near-surface velocity observations, *Geophys. Res. Lett.*, *30*(22), 2164, doi:10.1029/2003GL018628.
Papa, F., F. Durand, W. B. Rossow, A. Rahman, and S. Bala (2010), Satellite altimeter-derived monthly discharge of the Ganga-Brahmaputra River and its seasonal to interannual variations from 1993 to 2008, *J. Geophys. Res.*, *115*, C12013, doi:10.1029/2009JC006075.
Philander, S. G. H. (1978), Instabilities of zonal equatorial currents, 2, *J. Geophys. Res.*, *83*(C7), 3679–3682, doi:10.1029/JC083iC07p03679.
Qu, T., S. Gao, and I. Fukumori (2011). What governs the North Atlantic salinity maximum in a global GCM?, *Geophys. Res. Lett.*, *38*(7), L07602, doi:10.1029/2011GL046757.
Ren, L., and S. Riser (2009), Seasonal salt budget in the northeast Pacific Ocean, *J. Geophys. Res.*, *114*, C12004, doi:10.1029/2009JC005307.
Reul, N., et al. (2014a), Sea surface Salinity observations from space with the SMOS Satellite: A new means to monitor the marine branch of the water cycle, *Surv. Geophys.*, *35*(3), 681–722.
Reul, N., B. Chapron, T. Lee, C. Donlon, J. Boutin, and G. Alory (2014b), Sea surface salinity structure of the meandering Gulf Stream revealed by SMOS sensor, *Geophys. Res. Lett.*, *41*, 3141–3148, doi:10.1002/2014GL059215.
Reverdin, G., E. Kestenare, C. Frankignoul, and T. Delcroix (2007), Surface salinity in the Atlantic Ocean (30S-50N), *Prog. Oceanogr.*, *73*, 311–340, doi:10.1016/j.pocean.2006.11. 004.
Riser, S. C., L. Ren, and A. Wong (2008), Salinity in Argo: A modern view of a changing ocean, *Oceanography*, *21*, 56–67.
Roemmich, D., M. Morris, W. R. Young, and J. R. Donguy (1994), Fresh equatorial jets, *J. Phys. Oceanogr.*, *24*(3), 540–558.
Salisbury, J., D. Vandemark, J. Campbell, C. Hunt, D. Wisser, N. Reul, and B. Chapron (2011), Spatial and temporal coherence between Amazon River discharge, salinity, and light absorption by colored organic carbon in western tropical Atlantic surface waters. *J. Geophys. Res.*, *116*, C00H02, doi:10.1029/2011JC006989.
Short, D. A., P. A. Kucera, B. S. Ferrier, J. C. Gerlach, S. A. Rutledge, and O. W. Thiele (1997), Shipboard radar rainfall patterns within the TOGA COARE IFA, *Bull. Am. Meteorol. Soc.*, *78*, 2817–2836.
Terray, L., L. Corre, S. Cravatte, T. Delcroix, G. Reverdin, and A. Ribes (2012), Near-surface salinity as nature's rain gauge to detect human influence on the tropical water cycle, *J. Clim.*, *25*(3), 958–977.
Vinogradova, N. T., and R. M. Ponte (2013), Clarifying the link between surface salinity and freshwater fluxes on monthly to interannual time scales, *J. Geophys. Res. Oceans*, *118*, 3190–3201, doi:10.1002/jgrc.20200.
Wijesekera, H. W., C. A. Paulson, and A. Huyer (1999), The effect of rainfall on the surface layer during a westerly wind burst in the western equatorial Pacific, *J. Phys. Oceanogr.*, *29*, 612–632.
Xie, P.-P., and P. A. Arkin (1997), Global precipitation: A 17-year monthly analysis based on gauge observations, satellite estimates, and numerical model outputs, *Bull. Am. Meteorol. Soc.*, *78*, 2539–2558. doi:10.1175/1520-0477(1997)078<2539:GPAYMA>2.0.CO;2.
Yu, L. (2010), On surface salinity skin effect under evaporation conditions and implications for remote sensing of ocean salinity, *J. Phys. Oceanogr. 40*, 85–102.
Yu, L. (2011), A global relationship between the ocean water cycle and near-surface salinity, *J. Geophys. Res.*, *116*, C10025, doi:10.1029/2010JC006937.
Yu, L., and X. Jin (2012), Buoy perspective of a high-resolution global ocean vector wind analysis constructed from passive radiometers and active scatterometers (1987-present), *J. Geophys. Res.*, *117*, C11013, doi:10.1029/2012JC008069.
Yu, L., and X. Jin (2014), A satellite-derived high-resolution ocean surface vector wind analysis (1987 onward). Part I: Insights on the synergy between scatterometers and radiometers, *J. Geophys. Res. Oceans*, *118*, 5353–5375, doi:10.1002/jgrc.20386.
Yu, L., and R. A. Weller (2007), Objectively analyzed air-sea heat fluxes (OAFlux) for the global ocean, *Bull. Am. Meteorol. Soc.*, *88*(5), 527–539.
Yu, L., X. Jin, and R. Weller (2008), Multidecade global flux datasets from the objectively analyzed air-sea fluxes (OAFlux) project: Latent and sensible heat fluxes, ocean evaporation, and related surface meteorological variables, *OAFlux Project Tech. Rep. OA-2008-01*, 64 pp, Woods Hole Oceanographic Institution, Woods Hole, Mass. [Available at http://oaflux.whoi.edu/pdfs/OAFlux_TechReport_3rd_release.pdf.]
Yueh, S. H., and J. Chaubell (2012), Sea surface salinity and wind retrieval using combined passive and active L-band microwave observations, *IEEE Trans. Geosci. Remote Sens.*, *50*(4), 1022–1032.